Results in Optics 15 (2024) 100622

Contents lists available at ScienceDirect

Results in Optics

journal homepage: www.sciencedirect.com/journal/results-in-optics

Optimizing microlens arrays for incoherent HiLo microscopy

Ziao Jiao [a,b], Xi Chen [a], David Day Uei Li [a,*]

[a] Department of Biomedical Engineering, University of Strathclyde, Glasgow G1 1XQ, Scotland, UK
[b] Strathclyde Institute of Pharmacy and Biomedical Sciences, University of Strathclyde, Glasgow G4 0RE, Scotland, UK

ARTICLE INFO

Keywords:
HiLo microscopy
Simulation
Incoherent fluorescent imaging
Optically-sectioning

ABSTRACT

HiLo microscopy is a powerful, low-cost, and easily configurable technique for acquiring high-contrast optically-sectioned images. However, traditional HiLo microscopes are based on coherent light sources with diffusive glass plates or incoherent light sources with digital mirror devices (DMD) and spatial light modulators (SLM), which are more expensive. Here, we propose a new low-cost HiLo microscopy technique using MLAs and incoherent LED light sources. We simulated structured illumination (SI) patterns and HiLo image generation. To observe how MLAs affect HiLo images, we used three common MLAs with specific microlens pitch and numerical aperture (NA) to generate periodic illumination patterns. Our simulations concluded that the MLA's NA does not significantly affect HiLo images, and a larger lens pitch can bring a higher image contrast. However, there is an optimized lens pitch. If the lens pitch is equal to or higher than 140 μm, artifacts are observed in HiLo images. Based on our simulations, employing the cross-type MLA with a 0.01NA and a period of 120 μm yields the optimal HiLo image (94.6 % contrast). In our quantitative analysis with the traditional HiLo, where SI patterns were set with the same period, we calculated the SSIM index between each HiLo-Ground Truth image pair. The cross-type MLA HiLo performed slightly better (SSIM = 0.9554) than the traditional HiLo (SSIM = 0.9396). However, when using the hexagon-type MLA, artifacts were evident in the final HiLo image (SSIM = 0.9054). The cylinder-type MLA HiLo result (SSIM = 0.9366) is similar to the traditional HiLo. To our knowledge, this is the first numerical study about MLA-based HiLo microscopy. This study can benefit researchers using MLAs and incoherent light sources to configure their low-cost HiLo microscopes.

1. Introduction

HiLo is a widefield fluorescence microscope with an optical-sectioning (OS) function. It is a robust method for rejecting background noise and acquiring high-resolution OS images (Mertz and Kim, 2010; Schniete et al., 2018). HiLo can reveal fast biological processes in neuron cells (Lauterbach et al., 2015; Shi et al., 2019), discover 3D cell mechanical properties by rejecting out-of-focus signals (Kole et al., 2012), improve retinal image quality (Zhou et al., 2014), and realize 3D image cytometers (Choi et al., 2015). Besides these biomedical applications, HiLo can measure engineering microstructure surface profiles (Kang et al., 2018). HiLo's configuration is like widefield epi-fluorescence microscopy (Fig. 1). The only difference is that in HiLo, the illumination light is adjusted for generating patterns on the sample plane. Any widefield epi-fluorescence microscopy can be refitted to HiLo for optically-sectioned imaging by changing the illumination path. Compared with OS microscopy techniques such as confocal (Jonkman et al., 2020), two-photon (Helmchen and Denk, 2005), and light sheet microscopy (Andilla et al., 2018), HiLo does not need pinhole assignments, an expensive laser module, and dual objective lenses for illumination and excitation (Mertz, 2011). Similar to structured illumination (SI) microscopy, the light source in HiLo project a specific SI pattern to the in-focus sample plane. However, only two images are required for HiLo to reconstruct high-contrast OS images (Lim et al., 2011) instead of three images for the OS SI microscope (Wilson et al., 1997), one acquired with widefield illumination and the other with SI. With deep learning algorithms and advanced image processing, HiLo can now realize OS imaging using only one image (Chen et al., 2021; Hu et al., 2022). All these properties make HiLo relatively low-cost and easy to operate.

There are two common ways to obtain SI patterns in HiLo: 1) using a coherent light source with a diffuser (Ventalon and Mertz, 2005; Chu et al., 2008) to create speckle patterns or 2) using an incoherent light source with diffraction optical devices (Shi et al., 2019; Sanchez-Ortiga et al., 2018) to develop periodic patterns. However, coherent light sources, spatial light modulators (SLMs), and digital mirror devices

* Corresponding author.
E-mail address: David.li@strath.ac.uk (D. Day Uei Li).

https://doi.org/10.1016/j.rio.2024.100622
Received 1 November 2023; Received in revised form 10 January 2024; Accepted 2 February 2024
Available online 16 February 2024

(DMDs) increase the cost and system complexity.

Here, we proposed a new method that uses microlens arrays (MLAs) and uncoherent LED sources to reduce the cost and complexity of HiLo microscopy systems. As diffractive optical elements, MLAs can also modulate light into different patterns. Researchers have exploited lithography (Chang et al., 2004) and laser etching techniques (Lim et al., 2006) to fabricate MLAs quickly. Moreover, the molding method can also produce PDMS and PMMA-based MLAs (Kuo et al., 2017).

To the best of our understanding, there is currently no comparable approach for achieving HiLo microscopy utilizing MLAs and incoherent LED sources. Selecting suitable MLAs with appropriate physical parameters poses a challenge. Without theoretical guidance on choosing appropriate MLAs for achieving optimal HiLo microscopy performance, conducting experiments can become a time-consuming and challenging task. To address this issue, we have undertaken a numerical simulation study to evaluate the feasibility of the proposed method, offering an alternative to the direct execution of time-consuming experiments. Through simulations, we aim to identify specific MLAs with suitable parameters for practical HiLo microscopy to achieve optimal results. These findings will provide valuable insights for future experiments, streamlining the process and expediting the realization of MLA HiLo microscopy.

We first simulated how MLAs generate periodic illumination patterns on the illuminated sample volume. According to several studies about MLAs fabrication (Yuan et al., 2018; Sohn et al., 2019), we chose the three most common types of MLAs here: the cross-, cylinder-, and hexagon-types (Fig. 1). We examined how MLA's NA and its microlens pitch affects the spatial distribution of these illumination patterns. Then we generated a simulated fluorescent block, multiplying it with the MLA-generated illumination pattern and using the HiLo algorithm to obtain high-contrast optical-sectioning images. To balance the computational efficiency and mesh fineness, we tuned MLA's NA within a small range (0.006–0.01). The microlens pitch is set from 60 μm to 140 μm with a 20 μm step. After passing through the optical illumination path with 0.1 times magnification, the illumination pattern period is from 6 μm to 14 μm with a 2 μm step.

We discovered from the simulation results that the HiLo image contrast is not significantly affected by MLA's NA but still has a minor enhancement with a higher NA. Noticeably, the relationship between the microlens pitch and image contrast is more prominent. Moreover, a higher period can enhance the image contrast, but if the illumination period is 14 μm/period, the contrast deteriorates again. We also examined three MLA types to discover how pattern distribution affects image quality. Three kinds of MLAs perform similarly, except the illumination period reaches its optimal value (12 μm/period), and the cross-type MLA performs better than the others. We can obtain the best results using the cross-type MLA with 0.1NA and a pitch of 120 μm. Finally, we calculated the structure similarity (SSIM) between each HiLo image and the ground truth. The cross-type MLA HiLo performed slightly better (SSIM = 0.9554) than the traditional HiLo (SSIM = 0.9396). Although the enhancement is only 2 %, the proposed method is more cost-effective. We believe this numerical study can encourage more theoretical studies and the future development of low-cost MLA-based HiLo microscopes.

2. Theory

2.1. Fundamentals of HiLo microscope

The mathematic deduction and theoretical model of HiLo are reported in detail else (Lim et al., 2011; Ventalon and Mertz, 2005; Chu et al., 2008; Mertz and Ventalon, 2006; Heintzmann et al., 2007). Therefore we only describe it briefly. In HiLo, two images combine an optical-sectioning image ($I_{HiLo}(u,v)$):

$$I_{HiLo}(u,v) = I_{Hi}(u,v) + \eta I_{Lo}(u,v) \tag{1}$$

where $I_{Hi}(u,v)$ is the in-focus high-frequency image, $I_{Lo}(u,v)$ is the in-focus low-frequency image, and u,v are spatial coordinates. The parameter η can avoid discontinuities in the frequency domain, which can be calculated by (Santos et al., 2009):

$$\eta = \frac{HP_{k_c}}{LP_{k_c}} \tag{2}$$

where HP_{κ_c} and LP_{κ_c} are Gaussian high-pass and low-pass filters, respectively, and k_c, the cut-off frequency, should be less than or equal to the frequency of the structured illumination pattern. LP_{κ_c} is complementary to HP_{κ_c}. Because $I_{Hi}(u,v)$ is intuitively axially resolved, it can be acquired easily by:

$$I_{Hi}(u,v) = \mathscr{F}^{-1}\{HP_{k_c}[I_u(k_u,k_v)]\} \tag{3}$$

where $I_u(k_u,k_v)$ is the captured image in the frequency domain under uniform illumination and $\mathscr{F}^{-1}\{\}$ is the inverse Fourier operator. To get $I_{Lo}(u,v)$, which cannot be axially resolved, we need a weighting function to select the in-focus portion of $I_u(u,v)$ below the cut-off frequency. First, we get a bias-free difference image $I_\Delta(u,v)$ by subtracting $I_s(u,v)$, the captured image in the spatial domain under structured illumination, from $I_u(u,v)$:

$$I_\Delta(u,v) = I_u(u,v) - I_s(u,v) \tag{4}$$

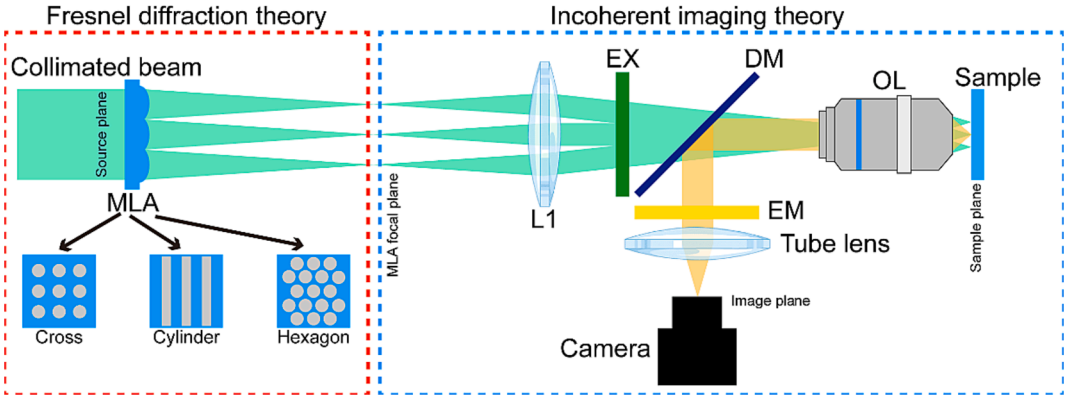

Fig. 1. The physical model of this study. Red and blue dashed rectangles denote physical theories used in different parts. We used three different MLAs to generate different illumination patterns. This optical path is for structured illumination. The uniform illumination can be easily obtained by removing the MLA, and the collimated beam can be focused on the back pupil plane of the OL by L1. For simplicity, we denote four planes in the figure (source plane, MLA focal plane, sample plane, and image plane), which are the same as Fig. 2. (MLA: microlens array; L1: convex lens; EX: excitation filter; DM: dichroic mirror; OL: objective lens; EM: emission filter). (For interpretation of the references to color in this figure legend, the reader is referred to the web version of this article.)

where $I_u(u,v)$ and $I_s(u,v)$ are the captured images under uniform and structured illumination in the spatial domain. According to Eq. (4), we can estimate the illumination-induced contrast $C(u,v)$ by:

$$C(u,v) = \sigma\{I_\Delta(u,v)\} \tag{5}$$

where σ{} means the standard deviation. According to Eq. (4) and Eq. (5), we can guarantee that the modulated component is locally centered about zero and make the evaluation insensitivity to differences in the global illumination profile (Ford et al., 2012). Then we weighted $I_u(u,v)$ with $C(u,v)$ and input it to the low-pass filter to acquire $I_{Lo}(u,v)$:

$$I_{Lo}(u,v) = \mathscr{F}^{-1}\{LP_{k_c}[C(k_u,k_v)I_u(k_u,k_v)]\} \tag{6}$$

where $C(k_u,k_v)$ is $C(u,v)$ in the frequency domain.

2.2. Theory of pattern projection and image formation

To study how MLAs affect the image quality of a HiLo microscope, we give a detailed mathematic deduction about structured illumination and image formation. For efficiency, we performed multiplications in the spectral domain instead of convolutions in the spatial domain. Fig. 1 illustrates the physical model of this study. An MLA modulates the collimated beam and forms a specific pattern on its focal plane. We use the Fresnel diffraction theory in this part. To create different patterns, we used three common types of MLAs (cross-, cylinder- and hexagon types). The illumination part of the 4f microscope system (L1 and OL) conjugates the illumination pattern to the sample plane, and the camera captures the excited fluorescent signal through the imaging part of the 4f microscope system (OL and Tube lens). We used the incoherent imaging theory in the illumination and imaging parts.

Firstly, let us see the image formation on the image plane. Fig. 2 is the coordinate system for a mathematical deduction. The image acquired under structured illumination is:

$$I_{4s}(u,v) = \sum_{z_i=0}^{n}\iint PSF_{em}(u-\mu, v-\sigma)\,|_{z=z_i} I_3(\mu,\sigma,z_i)O(\mu,\sigma,z_i)d\mu d\sigma \tag{7}$$

where PSF_{em} is the 2D emission point spread function with a defocus term (different z). O and I_3 are the 3D objects and illumination distribution, respectively, and z_i is the defocus distance between the focus and target plane ($z_i = 0$ is in focus). To obtain the intensity distribution on the image plane, we convoluted the corresponding structure-illuminated sample plane for each slice with a defocused PSF_{em}, and summed them up from $z_i = 0$ to $z_i = n$. When $I_3(\mu,\sigma,z_i)$ is 1 for different z_i, we can obtain the image under uniform illumination ($I_{4u}(u,v)$). For simplicity, we assume the imaging system is telecentric and has unit magnification. From Eq. (6), $I_3(\mu,\sigma,z_i)$ can determine the final HiLo image.

The incident beam is assumed to be a monochromatic plane wave, and we only consider the distribution inside each microlens of the MLA. Here, we consider the cross-type MLA and the amplitude distribution before the MLA can be written as:

$$U_1(\xi,\eta) = \sum_i\sum_j circ\left[\frac{\sqrt{(\xi-id)^2+(\eta-jd)^2}}{w}\right] = \begin{cases} 1 inside each microlens \\ 0 otherwise \end{cases} \tag{8}$$

where w is the radius of each microlens, d is the distance of the neighboring microlens, i and j denote the indices of microlenses in two perpendicular directions ($i = 0$, $j = 0$ for central microlenses). The phase transformation of the cross-type MLA can be written as:

$$\phi(\xi,\eta) = \sum_i\sum_j exp\left\{-j\frac{2\pi}{\lambda_{ex}}\left[(\xi-id)^2+(\eta-jd)^2\right]\right\}, and d > 2w \tag{9}$$

where λ_{ex} is the illumination wavelength. According to Eq. (8) and Eq. (9), we can obtain the Fraunhofer diffraction pattern at the focal plane of the MLA. For incoherent imaging, we only care about the distribution of the illumination intensity; thus, the intensity at the MLA focal plane is (Goodman, 2005):

$$\begin{aligned} I_2(x,y) &= \left|U_2(x,y)U_2^*(x,y)\right| \\ &= \sum_i\sum_j\left(\frac{w^2}{\lambda_{ex}f}\right)^2\left\{\frac{J_1\left[\frac{2\pi w}{\lambda_{ex}f}\sqrt{(x-id)^2+(y-jd)^2}\right]}{\frac{w}{\lambda_{ex}f}\sqrt{(x-id)^2+(y-jd)^2}}\right\}^2 \end{aligned} \tag{10}$$

where J_1 is the first-order Bessel function.

For the HiLo microscope, we use the incoherent imaging theory to conjugate this pattern to the sample plane for structured illumination. We assume the blue dashed rectangular region in Fig. 1 is a telecentric configuration. The objective lens is used for illuminating and imaging the samples. According to the incoherent imaging theory, the intensity distribution on the sample plane is:

$$\begin{aligned} I_3(\mu,\sigma,z)\,|_{z=z_i} &= \iint |h(\mu-x,\sigma-y)\,|_{z=z_i}|^2 \times I_{3-geometric}(\mu,\sigma)dxdy \\ &= \iint |h(\mu-x,\sigma-y)\,|_{z=z_i}|^2 \times I_2(Mx,My)dxdy \end{aligned} \tag{11}$$

where $h|_{z=z_i}$ is the coherent impulse response function for the defocus distance z, the coordinate (μ,σ) is related with $(\mu = Mx, \sigma = My)$, and M is the lateral magnification. $z_i = 0$ is the in-focus plane. $I_{3-geometric}(\mu,\sigma)$ is the scaled ideal geometric image copy of $I_2(x,y)$. Due to the telecentric configuration, $I_{3-geometric}(\mu,\sigma)$ remains the same for different z distances. Thus, Eq. (11) can be rewritten as:

$$I_3(\mu,\sigma,z)\,|_{z=z_i} = \mathscr{F}^{-1}\left\{\mathscr{H}_{ill}(f_\mu,f_\sigma)\,|_{z=z_i} G_g(f_\mu,f_\sigma)\right\} \tag{12}$$

where $\mathscr{H}_{ill}(f_\mu,f_\sigma)\,|_{z=z_i}$ is the illumination optical transfer function (OTF) at a defocus distance z_i. According to (FitzGerrell et al., 1997):

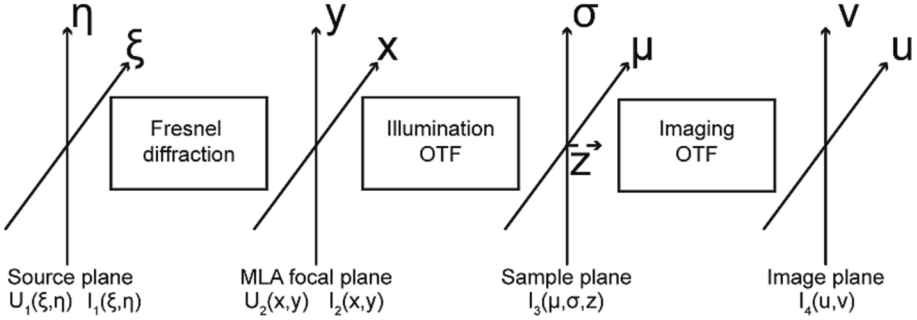

Fig. 2. Coordinate system of illumination and imaging process.

$$\mathscr{H}_{ill}(f_\mu, f_\sigma) = circ\left(\frac{\sqrt{f_\mu^2 + f_\sigma^2}}{f_0}\right) exp\left\{j\pi z_i \lambda_{ex}\left(f_\mu^2 + f_\sigma^2\right)\right\} \quad (13)$$

where z_{xp} and w_{xp} are the exit pupil distance and exit pupil radius, respectively, and f_0 is $\lambda z_{xp}/w_{xp}$. The sign assignment of wavefront error is the same as (FitzGerrell et al., 1997). For convenience, we recall it here. In Fig. 3, when the defocused wavefront converges to the right side of the ideal focus point and the corresponding defocused wavefront on the left side, W_d and z_i are positive.

According to the analytic expression for the OTF of a circular asymmetric optical system with defocused aberration, which was first given by Hopkins (Hopkins, 1955), the OTF of the HiLo illumination can be rewritten as (STOKSETH PA, Properties of a Defocused Optical System*, JOSA, Vol. 59, Issue 10, Pp., 1969):

$$\mathscr{H}_{ill}(f_\mu, f_\sigma)\big|_{z=z_i} = \mathscr{H}_{ill}(\rho) = \begin{cases} 2\left(1 - 0.69\rho + 0.076\rho^2 + 0.043\rho^3\right)\left[\frac{J_1(\alpha - 0.5\alpha\rho)}{(\alpha - 0.5\alpha\rho)}\right], & |\rho| < 2 \\ 0, & |\rho| \geq 2 \end{cases} \quad (14)$$

where $\alpha = \frac{2\pi w_{xp}^2 z_i}{\lambda_{ex} z_{xp}^2}\rho$, $\rho = \sqrt{s^2 + \tau^2}$, s and τ are normalized spatial frequency components defined as $\lambda_{ex} z_{xp} f_\mu / w_{xp}$ and $\lambda_{ex} z_{xp} f_\sigma / w_{xp}$, respectively.

We calculated the Fourier transform of I_2 (Mx,My) to obtain $G_g\left(f_\mu, f_\sigma\right)$ in Eq. (12). Recalling Eq. (10) and using the autocorrelation theorem, we can rewrite the the 3D illumination pattern on the sample volume as:

$$I_3(\mu, \sigma, z)\big|_{z=z_i} = \mathscr{F}^{-1}\left\{\mathscr{H}_{ill}(\rho) \times ACF\mathscr{F}\left\{\exp\left[\frac{j\pi M^2(x^2 + y^2)}{\lambda_{ex} f}\right]\right\} \otimes \sum_i \sum_j circ\left[\frac{\sqrt{[M(x - id)]^2 + [M(y - jd)]^2}}{Mw}\right]\right\} \quad (15)$$

where $ACF<>$ is the correlation operator and $\otimes$ is the convolution operator.

From Eq. (7), we can rewrite it in the spectrum domain:

$$I_{4s}(u, v) = \sum_{z_{i=0}}^{n} \mathscr{F}^{-1}\left\{\mathscr{H}_{ima}(\rho)\mathscr{F}\left\{O(\mu, \sigma, z_i) I_3(\mu, \sigma, z)\big|_{z=z_i}\right\}\right\} \quad (16)$$

where $\mathscr{H}_{ima}(\rho)$ is the same as Eq. (14), except that the emission wavelength λ_{em} substitutes the illumination wavelength λ_{ex}.

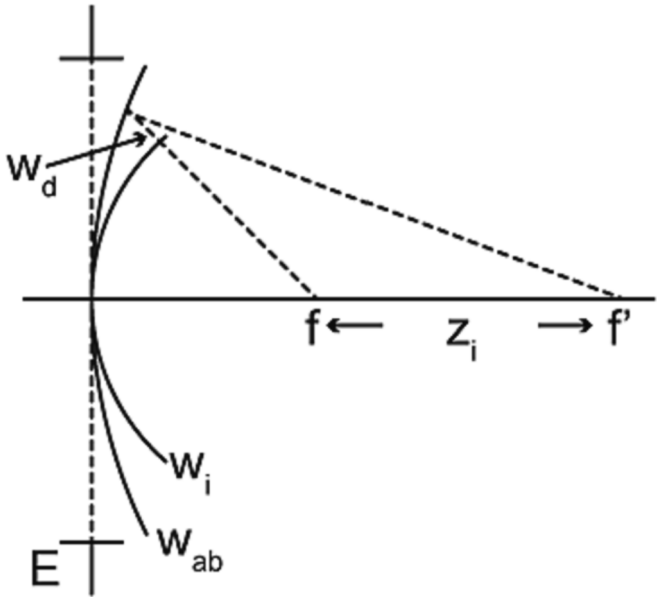

Fig. 3. Illustration of defocus. E is the exit pupil, wavefront w_i converges to the focus point f, and the defocus wavefront w_{ab} is centered on the axis at the defocus point f'.

3. Simulations

3.1. 3D illumination pattern on the sample volume

We simulated different 3D illumination patterns on the sample volume. The illumination wavelength is 520 nm, the illumination NA is 0.5, and the sample volume is 200*200*100 μm (width*length*height). We set MLA's NA from 0.006 to 0.01 with a step of 0.001. Each microlens is 50 μm in diameter; the microlens pitch (distance between adjacent microlens) is from 60 μm to 140 μm with a 20 μm step. Fig. 4 shows several normalized 3D illumination patterns created by different MLAs. The x-y section shows the intensity distribution on the focus plane (z_i = 0μm), and the x-z section shows the axial intensity distribution of the central slice (y = 0) from z_i = 0μm to z_i = 100μm. The magnification of the illumination light path is 0.1; therefore, the pattern period on the sample plane in Fig. 4 is ten times smaller than MLA's lens pitch (6 μm, 10 μm, and 14 μm).

When using MLA to create SI on the sample, its microlens pitch and NA determine the modulation depth (MD). Fig. 5 shows horizontal line profiles of the focus plane (x-y section, y = 0 in Fig. 4). In the same MLA type, a higher microlens pitch increases MD. Beyond that, increasing NA also causes a higher MD. According to Eqs (8) and (18), the intensity distribution formed by each microlens at the sample plane is an Airy pattern. Therefore, if the period (corresponding to MLA's microlens pitch) and NA are too large, the side lobes of each focus point will sum up and cause oscillation (purple arrows in Fig. 5). We define MD as MD (%)=(I_{max}-I_{min})/(I_{max} + I_{min}), where I_{max} and I_{min} are the profile's maximum and minimum intensities. Fig. 6 shows relationships between MD, NA, and the period for different MLAs. As expected, increasing the period and NA can obtain higher MD rates. Because of the structure's similarity, illumination patterns formed by the cross-type and hexagon-type MLAs have similar MD rates and trends. When the period and the NA are both low, cylinder-type MLAs can create patterns with higher MD rates (>50 %).

3.2. The axial resolution of illumination patterns on the sample volume

The relationship between MLA and axial resolution of illumination patterns on the sample volume is also numerically studied. Fig. 7 shows the central (x = y = 0) axial line profiles of illumination patterns on the sample volume. The axial range is 0 μm to 10 μm. Purple arrows denote the first global minimal value along the axial line. We denoted this position as z_{min}, whose corresponding intensity is I_{z-min}.

Similarly, the in-focus position z_{max} has the maximum intensity I_{z-max}. δI is $I_{z-max} - I_{z-min}$. To quantify the axial resolution, we defined the axial FWHM as $2z_{FWHM}$. z_{FWHM} is the axial position when the axial intensity is half the difference between maximum and first side lobe minimum intensity. For clearance, these definitions are annotated in Fig. 7, center picture. Fig. 7 shows that Cross-type and Hexagon-type line profiles are similar, and Cylinder-type lines are always higher than the others. As expected, a higher NA increases δI. Beyond that, z_{min} seems only determined by the period of the illumination pattern, and a higher period would bring a larger z_{min}. We did a quantitative analysis to discover how the MLA type affects the axial resolution of illumination patterns. Table 1. summarizes how z_{min} behaves in terms of the MLA type, the periods, and NA. Obviously, z_{min} depends only on the period of the illumination pattern.

$$MD(\%) = \left(I_{max} - I_{min}\right) / \left(I_{max} + I_{min}\right)$$

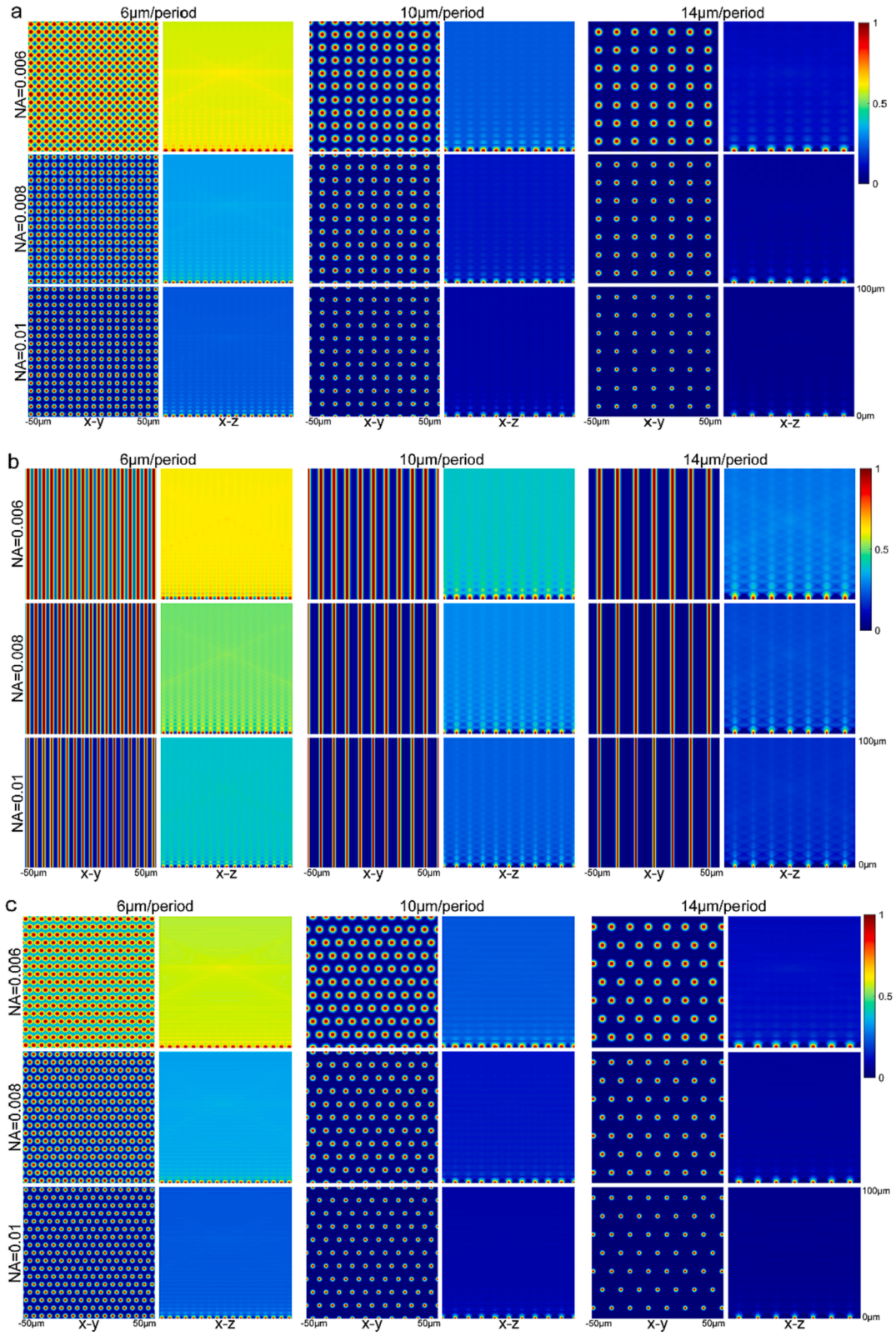

Fig. 4. 3D illumination intensity distribution on the sample volume created by cross-type (a), cylinder-type (b), and hexagon-type (c) MLAs. Each picture is self-normalized, and the NA is MLA's numerical aperture. The period is the distance between adjacent focus points on the x-y focus plane, which MLA creates.

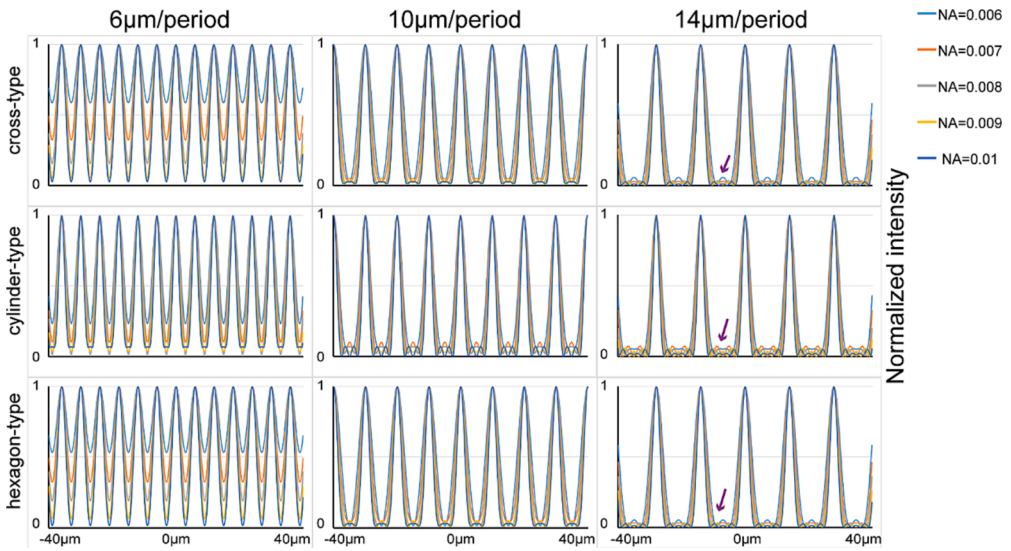

Fig. 5. Horizontal line profiles of illumination patterns on the in-focus plane (x-y section, y = 0). Different color lines represent microlens.

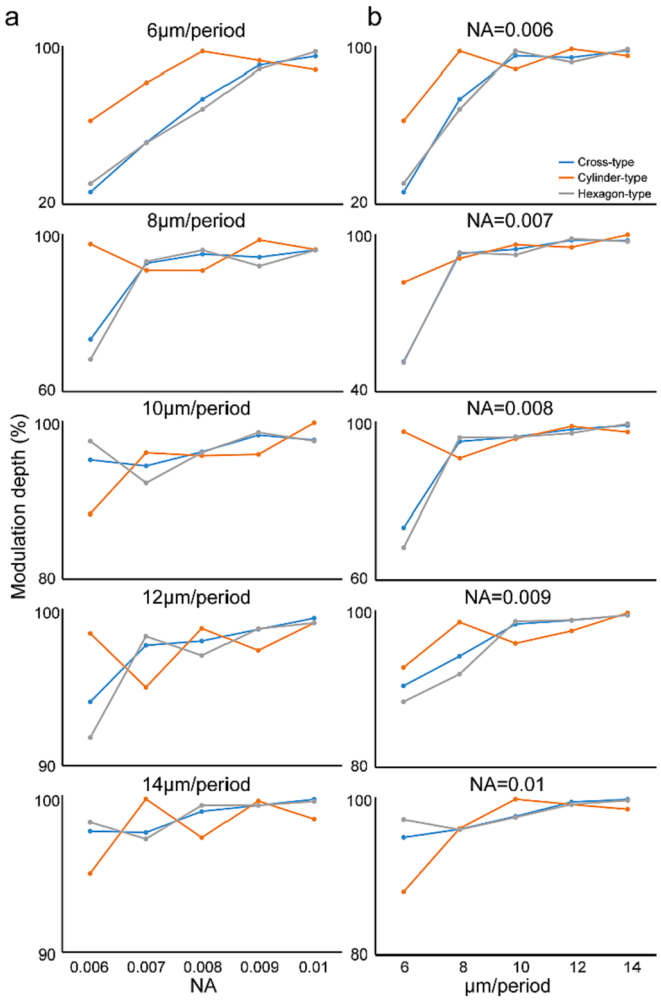

Fig. 6. Relationships between MD and microlens NA (a), MD and pattern period (b). Different color lines represent MLA's type. Scales are different for better visualization.

Fig. 8 shows the axial resolution (z_{FWHM}) changing with different MLA's NA and illumination pattern periods. The higher the MLA's NA or, the lower the illumination pattern period, the better the axial resolution. In Fig. 8(a), the gradient is steeper with a higher period. On the other hand, the gradient is gentle with higher NA in Fig. 8(b). In addition, we found that the cylinder-type MLA has worse axial resolution when compared to the others. Because the cylinder-type MLA creates periodic features on the focus plane only in a one-dimensional direction. The intensity variation only exists in one direction; however, in cross-type and hexagon-type, this variation is in two orthogonal directions, and the propagating light field changes more quickly. Therefore, z_{FWHM} in cross- and hexagon-types are smaller than z_{FWHM} in the cylindrical type.

3.3. HiLo imaging simulation

To understand the effects of MLA-generated SI patterns on the HiLo image, we modeled a fluorescent block for simulating incoherent widefield and HiLo imaging (Fig. 9(a) and (b)). According to Eq. (6), we first multiplied the sample with a specific 3D illumination pattern. Then, we used the incoherent imaging theory to acquire SI images on the camera plane. Similarly, we used the same method to obtain widefield images (Fig. 9(c)), except that the fluorescent block was multiplied by the all-one matrix instead of the MLA-generated SI pattern. In the simulations, we set the illumination and the imaging NA to 0.5, and the excitation and emission wavelengths are 520 nm and 580 nm, respectively. The magnification in the illumination light path is 10, and 1 in the imaging light path.

Fig. 10 shows images of the fluorescent block on the camera plane. SI columns are images under SI illumination, and HiLo columns show final HiLo pictures. The widefield image used as input for HiLo algorithms is shown in Fig. 9(c). In Fig. 10(a), the fluorescent target is excited by a cross-type illumination pattern, and others are excited by cylinder-type (Fig. 10(b)) and hexagon-type (Fig. 10(c)). When the pattern's period is 14 μm/period, we found uneven artifacts on these HiLo images (white arrows). Especially when the pattern is the hexagon type (Fig. 10(c)), artifacts seem the worst. The cross-type pattern also generates recognizable ununiform intensity (Fig. 10(a)). In cylinder-type patterns, these imperfections are the mildest. Artifacts are caused by side lobes that sum up and cause oscillations (Purple arrows in Fig. 5). With larger lens pitch and higher NA, more side lobes will exist between each microlens, and the oscillation will become more serious. These artifacts are the mildest in cylinder-type patterns because side lobes and oscillation only exist in

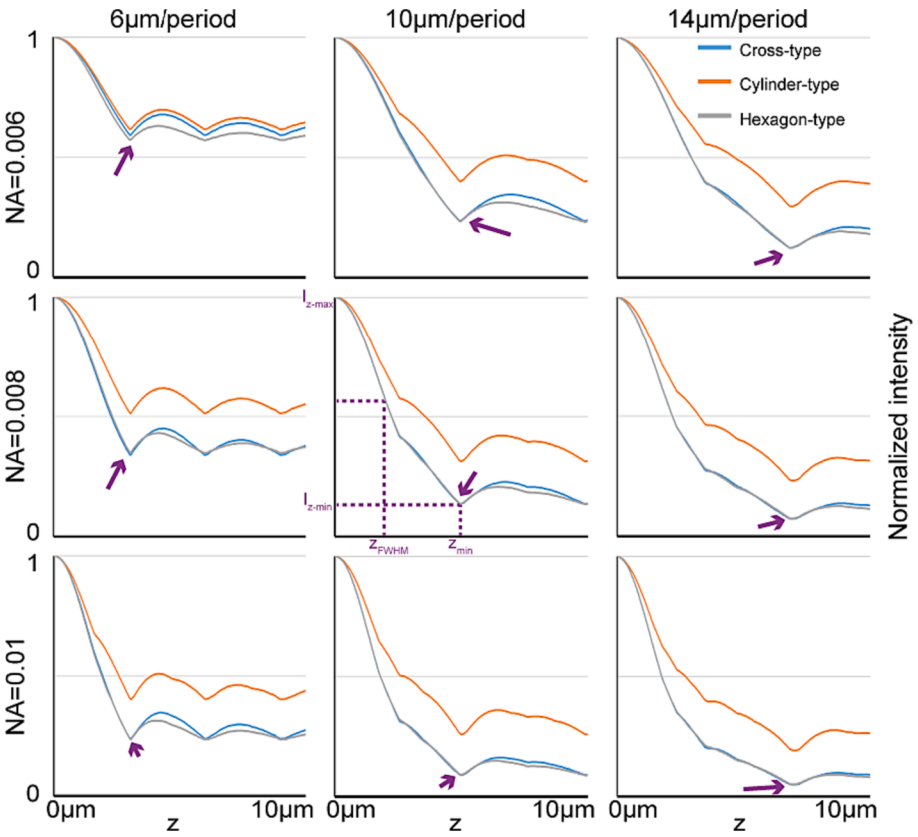

Fig. 7. Axial line profiles of illumination patterns at x = y = 0. The purple arrow denotes the first global minimal position along the axial line. The central picture shows detailed positions about z_{min}, z_{FWHM}, I_{z-min}, and I_{z-max}. (For interpretation of the references to color in this figure legend, the reader is referred to the web version of this article.)

Table 1
The value of z_{min} (μm as the unit) in terms of the MLA type, the period, and NA. Cro, cyl, and hex denote cross-type, cylinder-type, and hexagon-type MLAs.

Period / NA	6 μm/period			8 μm/period			10 μm/period			12 μm/period			14 μm/period		
	cro	cyl	hex	cro	cyl	hex	cro	cyl	hex	cro	cyl	hex	cro	cyl	hex
0.006	3	3	3	4	4	4	4.95	4.95	4.95	5.85	5.85	5.85	6.8	6.9	6.8
0.007	3	3	3	4	4	4	4.95	4.95	4.95	5.85	5.95	5.85	6.9	6.9	6.8
0.008	3	3	3	4	4	4	4.95	4.95	4.95	5.95	5.95	5.85	6.9	6.95	6.9
0.009	3	3	3	4	4	4	4.95	4.95	4.95	5.95	6	5.95	6.95	6.95	6.9
0.01	3	3	3	4	4	4	4.95	5.05	4.95	5.95	6	5.95	6.95	7	6.95

one dimension but two dimensions in both cross-type and hexagon-type. Furthermore, cross-type has fewer artifacts when compared with hexagon-type since its two-dimensional patterns are orthogonal and can be decomposed into *x* and *y* directions. However, in hexagon-type, these artifacts are correlated. To quantitively analyze how MLA-generated illumination patterns affect HiLo images, we traced line profiles on each HiLo image (Red line in Fig. 10(a). Same tracing positions in all HiLo images.).

In Fig. 10, these images are similar; therefore, captured images of 8 μm/period, 12 μm/period, NA = 0.007, and NA = 0.009 are not shown. However, we traced line profiles on every condition, NA from 0.006 to 0.01 with a step of 0.001, and period from 6 μm/period to 14 μm/period with 2 μm/period step. According to the line profiles shown in Fig. 11, the NA of MLA does not seem to affect the quality of the final HiLo image. Fig. 11(a) (12 μm/period column) shows a minor contrast enhancement with a higher NA. However, some artifacts are created if the period is too high (14 μm/period). In Fig. 11(a), the contrast of the second and fourth lobes (purple arrows) is lower than others, and their trends become inverse (the higher the NA, the lower the contrast). In Fig. 11(b), we can see clearly that a higher period can enhance the final HiLo image contrast, and this tendency is more evident for the cross-type illumination. Like Fig. 11(a), artifacts appear when the period is 14 μm/period.

Furthermore, we recorded the normalized local maximum intensity of the middle lobe in Fig. 11. Table 2 shows how the intensity changes with different periods and NA. The period affects the intensity more significantly than MLA's NA. The best parameter setting is the cross-type pattern with 0.01NA and 12 μm/period.

Traditional HiLo microscopy employs binary square wave patterns—black and white periodic fringes—as SI patterns due to the inherent design of DMD chips (Ford et al., 2012; Hsiao et al., 2021; Shi and Kong, 2021). Consequently, we compared the proposed method with the binary SI HiLo microscopy. The target specimen was illuminated successively with binary, cross, cylinder, and hexagon SI patterns, as illustrated in Fig. 12a. For the binary scenario, we simulated traditional HiLo microscopy based on the principles of incoherent imaging theory.

Based on the optimal parameters obtained from the previous results (Table. 2), we configured the period of SI patterns and the NA of MLAs as 12 μm/period and 0.01, respectively. Fig. 12a shows the final optical

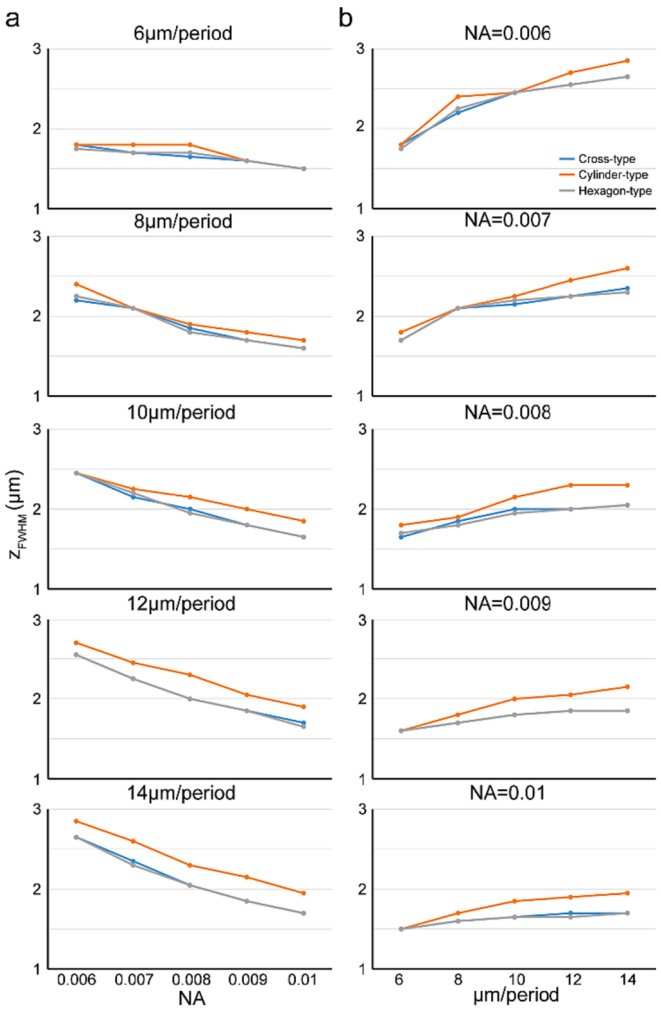

Fig. 8. Relationships between axial resolution (z_{FWHM}) and microlens NA (a), axial resolution (z_{FWHM}) and pattern period (b). Different color lines represent MLA's type.

sectioning results, illuminated by corresponding SI patterns. The structure similarity (SSIM) index of each HiLo image was calculated by using HiLo and ground truth images (Wang et al., 2004). For traditional HiLo, the SSIM can reach 0.9396 (0.8684 for widefield). The best result was obtained by using the cross-type SI pattern (SSIM = 0.9554). As expected, noticeable artifacts emerge when the hexagon-type SI pattern is employed. According to corresponding line profiles (Fig. 12b), while the distinctions are subtle, a slight improvement is discernible when utilizing cross-type SI patterns, particularly evident in the central lobe and its local minimum value. The local minimum of the central lobe cannot reach zero when the sample is illuminated by binary and cylinder patterns. The results based on the cylinder-type SI pattern are similar to the traditional HiLo microscopy because they have similar SI patterns.

4. Discussion and prospect

HiLo microscopy is a powerful and straightforward tool for optical sectioning. Here, we found that using an incoherent light source and MLA can also realize HiLo microscopy, and this configuration can reduce HiLo's cost and system complexity.

In this study, we choose three different MLA types (cross-, cylinder-, and hexagon-types) with different NA and the microlens pitch size as diffractive components to generate SI patterns. Firstly, we used the Fresnel diffraction theory to study how different MLAs affect SI patterns. The modulation depth increases with a higher NA when the microlens pitch is small enough. Similarly, the modulation depth increases significantly with a broader lens pitch in low NA situations. However, when NA (the microlens pitch) is too high, the modulation depth would not be affected by the microlens pitch (NA).

NA and the microlens pitch size need to be carefully chosen. A higher NA would minimize focus point size, and a higher period can lead these focus points side lobes to accumulate between each microlens, causing oscillations (Fig. 5 purple arrows). These oscillations will create artifacts on the final HiLo images (Fig. 10 red arrows). Here, we chose NA from 0.006 to 0.01 to prevent the point size is too small. In terms of other MLAs type, the cross-type and hexagon-type perform similarly, and the cylinder-type MLA can generate SI patterns with a better modulation depth when NA or the microlens pitch is low. We also discussed the axial resolution of SI patterns. As expected, when the microlens pitch lens is unavailable, a higher NA can deliver a better axial resolution. This trend is evident with a bigger microlens pitch. Conversely, the axial resolution becomes worse with a higher microlens pitch when NA is unaltered, and this phenomenon is more pronounced in low NA conditions. When MLA's parameters are the same, the cylinder-type MLA has the worst axial resolution, and the cross-type and the hexagon-type MLA perform similarly.

We multiplied the simulation-generated fluorescent block with SI patterns, using the incoherent imaging theory and HiLo algorithms to investigate the links between HiLo images and MLAs. We found fewer differences among these HiLo images with different MLA NAs than those with different MLA microlens pitches. This is because the period of SI patterns, not MLA's NA, causes a larger image standard deviation, which directly affects the final HiLo images (Eq. (5). Moreover, a large microlens pitch can introduce artifacts and ununiform intensity to final HiLo images because a higher pitch allows more side lobes oscillation exists between each microlens focus point. From quantitative analysis, we found that the hexagon-type MLA is the most susceptible to artifacts.

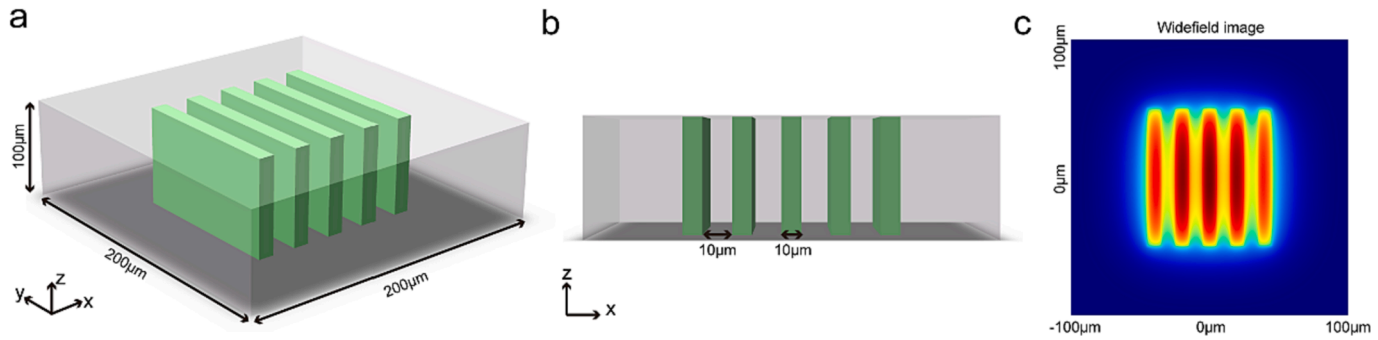

Fig. 9. Simulated fluorescent block for HiLo imaging (a and b). The green parts can be excited by 520 nm wavelength illumination. The residual grey transparent parts cannot create a fluorescent signal. The emission wavelength is 580 nm. (c) The self-normalized widefield image on the camera plane. (For interpretation of the references to color in this figure legend, the reader is referred to the web version of this article.)

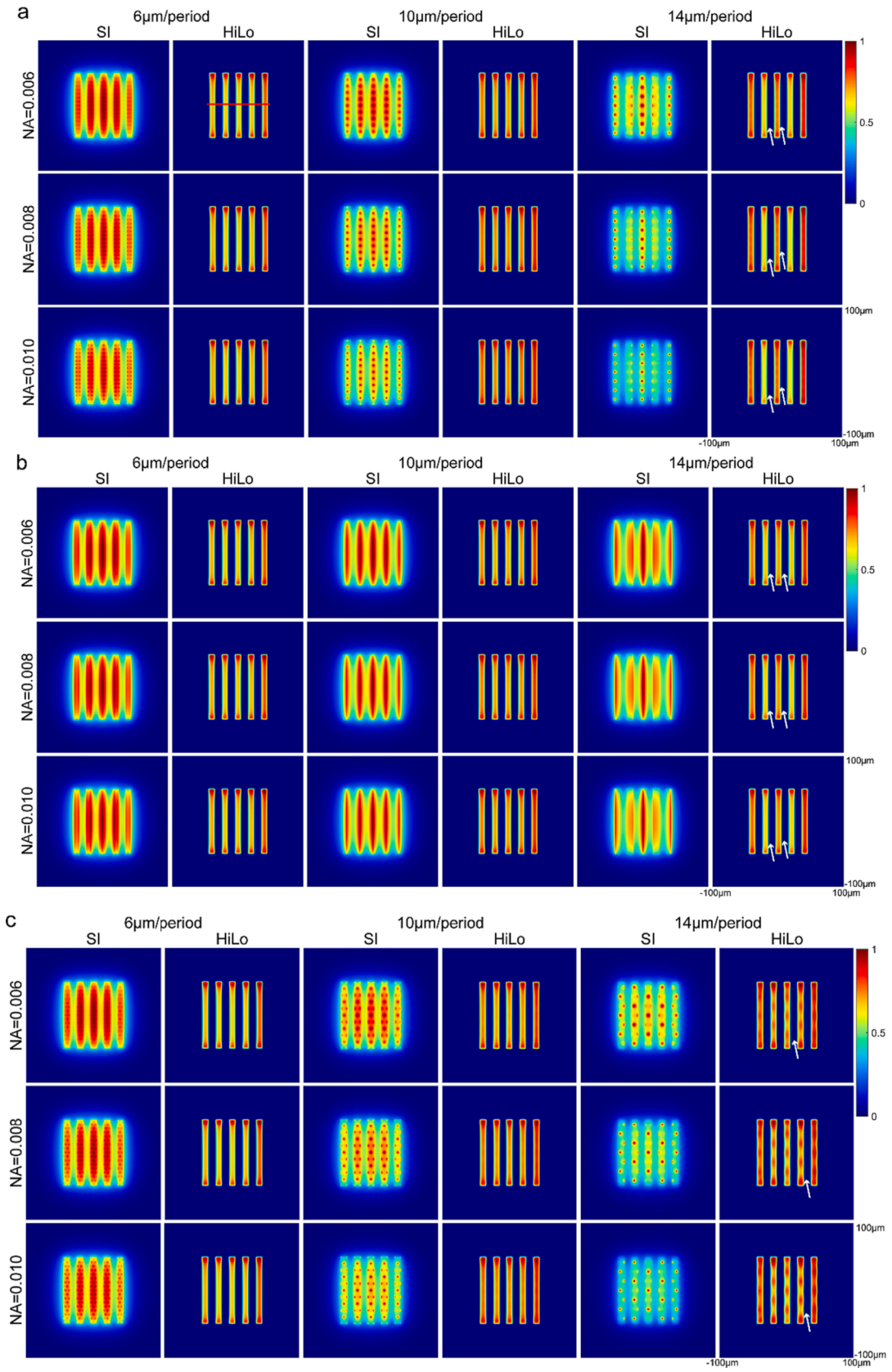

Fig. 10. Captured images on the camera plane. The corresponding widefield image is shown in Fig. 9(c). SI columns show images under different SI illumination. HiLo columns are the final HiLo images. Headlines are periods of corresponding illumination patterns. 8 μm/period and 12 μm/period are not shown. Different NAs are corresponding to MLA's numerical aperture. NA = 0.007 and NA = 0.009 are not shown. (a) Cross-type illumination pattern. (b) Cylinder-type. (c) Hexagon-type. Each image is normalized. White arrows depict imperfections.

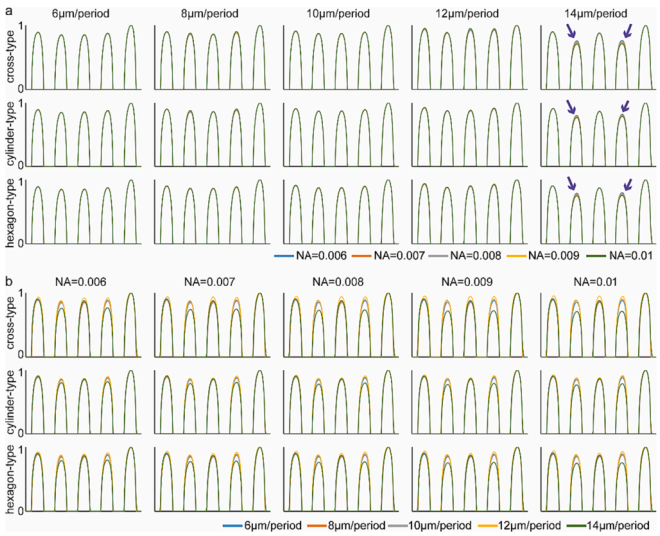

Fig. 11. Line profiles (along the red line in Fig. 10) of HiLo images under different illumination patterns. In (a), we can see that the NA of MLA does not significantly affect the image quality. Interestingly, when the period is 14 μm/period, the contrast of the second and fourth lobes (counted from left to right) is lower than others. (Depicted by purple arrows). The same phenomenon can be found in (b). In (b), the image contrast becomes better with a higher period, except 14 μm/period. (For interpretation of the references to color in this figure legend, the reader is referred to the web version of this article.)

Using the cross-type MLA with NA of 0.01 and the microlens pitch of 120 μm to generate SI patterns can obtain the best HiLo images. In the cylinder- and hexagon-types, the best parameter is NA = 0.01 with a 120 μm microlens pitch. Besides, due to the simplicity of corresponding periodic patterns, less oscillation can be found in cylinder-type-generated illumination patterns. We can obtain HiLo images with the mildest artifacts using the cylinder-type MLA.

Finally, we calculated the SSIM index between each HiLo image and the ground truth. The widefield image has the lowest SSIM (0.8684). The SSIM of traditional HiLo (0.9396) is lower than the SSIM of cross-type MLA HiLo (SSIM = 0.9554) but similar to cylinder-tyle MLA HiLo (SSIM = 0.9366). When using the hexagon-tyle MLA, the SSIM performs worst (0.9054). The proposed method can enhance the performance of traditional HiLo microscopy by 2 % at a lower cost.

Overall, in this study, we found that the best choice of our proposed method for HiLo imaging is using the cross-type MLA with 0.01NA and a 120 μm lens pitch to generate SI patterns. Nevertheless, when considering biological sample distribution, how to use cross-type MLA with proper parameters will be further studied. However, considering the similarities between the traditional HiLo and the cylinder-type MLA HiLo, using the cylinder-type MLA for HiLo microscopy is also a good choice for cost minimization.

5. Conclusion

In summary, we found that MLA is practical and cost-effective for generating structured illumination for HiLo microscopy. Our study shows how MLA's parameters (MLA's type, NA, and microlens pitch) affect final HiLo images. Simultaneously, we found the best MLA parameters in our study. To our knowledge, this is the first study about using proper MLAs to realize HiLo microscopy. A more detailed analysis will be conducted for further investigation, including a more comprehensive NA range, a larger microlens pitch, the ratio between NA and the lens pitch, and multiple microlens arrangements. Furthermore, we believe this study can guide more researchers to establish MLA-based HiLo microscope systems. Soon, such tools could help researchers acquire good-quality biomedical images and analyze them efficiently and cheaply.

Impact statement

This paper presents a new low-cost HiLo microscopy technique using MLAs and incoherent LED. We simulate structured illumination (SI) patterns and HiLo image generation based on Fresnel diffraction and incoherent imaging theories. To observe how MLAs affect HiLo images, we used three common MLAs (cross-, cylinder-, and hexagon type) with specific microlens pitch and numerical aperture (NA) to generate periodic illumination patterns. According to the detailed mathematical deduction and numerical simulation, we analyze how different MLAs affect SI patterns' appearance, modulation depth, and axial resolution. We also study how these SI patterns alter the final HiLo images' performance. We conclude that increasing MLA's lens pitch can enhance the HiLo image's contrast and optically-sectioned ability. However, this pitch size has a valve value. Beyond that, we also find that the hexagon-type MLA is the most susceptible to artifacts, and we can get HiLo images with the mildest artifacts using cylinder-type MLA. To our knowledge, this is the first study about using proper MLAs to realize HiLo microscopy.

Table 2
The normalized local maximum intensity of the middle lobe in Fig. 11.

Period / NA	6 μm/period			8 μm/period			10 μm/period			12 μm/period			14 μm/period		
	cro	cyl	hex	cro	cyl	hex	cro	cyl	hex	cro	cyl	hex	cro	cyl	hex
0.006	0.84	0.844	0.838	0.85	0.852	0.85	0.863	0.862	0.862	0.916	0.868	0.888	0.873	0.859	0.867
0.007	0.842	0.846	0.841	0.853	0.855	0.853	0.866	0.864	0.866	0.928	0.872	0.895	0.875	0.861	0.868
0.008	0.844	0.848	0.843	0.855	0.856	0.856	0.869	0.865	0.869	0.936	0.875	0.898	0.877	0.861	0.869
0.009	0.845	0.85	0.844	0.857	0.857	0.859	0.871	0.867	0.871	0.942	0.877	0.9	0.878	0.862	0.869
0.01	0.847	0.852	0.846	0.858	0.858	0.86	0.872	0.868	0.873	0.946	0.879	0.901	0.879	0.863	0.87

Abbreviations are the same in Table 1.

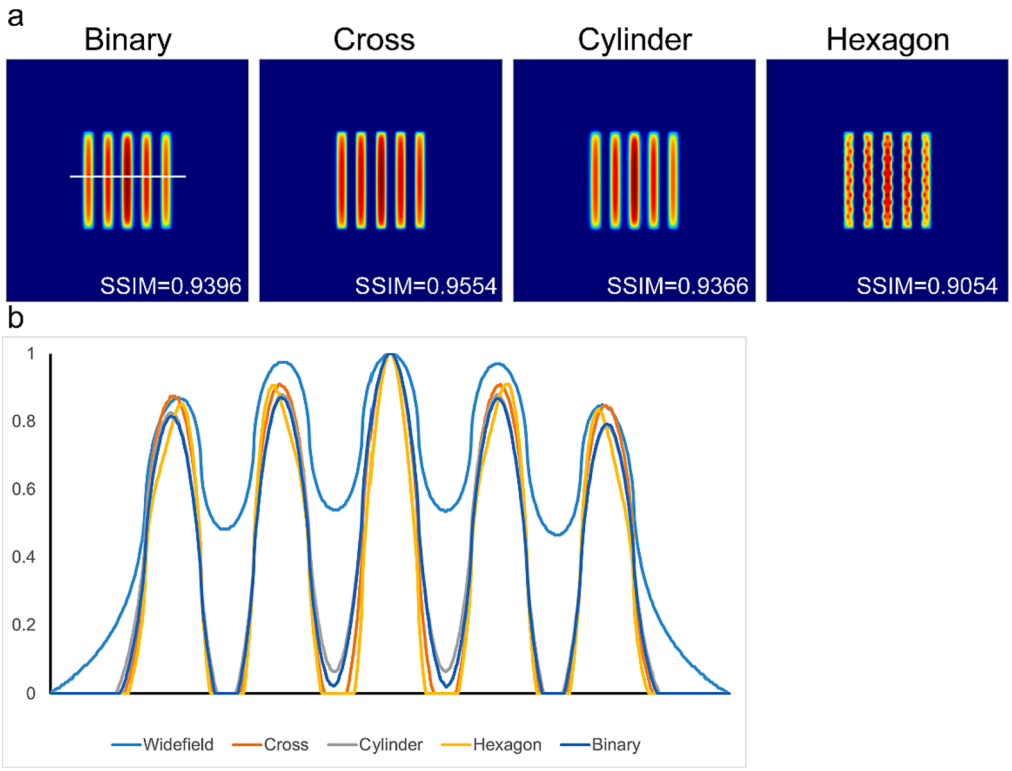

Fig. 12. Comparison of different HiLo images with different SI patterns. (a) All the SI patterns have the same period (12 μm/period). The 'Binary' image is the traditional HiLo microscopy result, and others are HiLo results based on different SI patterns as discussed before. The SSIM of each HiLo-Ground Truth pair are calculated (b) Corresponding line profiles depicted by the white line in (a).

The main innovations of this work are:

1. To our knowledge, this is the first numerical study about using proper MLAs to realize HiLo microscopy.
2. This study can guide a more detailed analysis for further investigation in the theoretical research field, including a more comprehensive NA range, a larger microlens pitch, the ratio between NA and the lens pitch, and multiple microlens arrangements.
3. This study can guide more researchers to establish low-cost MLA-based HiLo microscope systems in the experiment and engineering aspects.

CRediT authorship contribution statement

Ziao Jiao: Conceptualization, Data curation, Formal analysis, Funding acquisition, Investigation, Methodology, Validation, Writing – original draft, Writing – review & editing. **Xi Chen:** Investigation, Methodology, Writing – review & editing. **David Day Uei Li:** Funding acquisition, Investigation, Supervision, Writing – review & editing.

Declaration of competing interest

The authors declare that they have no known competing financial interests or personal relationships that could have appeared to influence the work reported in this paper.

Data availability

Data will be made available on request.

Acknowledgements

The research has been supported by the Engineering and Physical Sciences Research Council under EPSRC Grant: EP/T00097X/1, the Royal Society of Edinburgh, and the China Scholarship Council.

References

Andilla, J., Gualda, E.J., Olarte, O.E., Loza-Alvarez, P., 2018. Light-sheet microscopy: a tutorial. Advances in Optics and Photonics 10 (1), 111–179. https://doi.org/10.1364/AOP.10.000111.

Chang, S.-I., Yoon, J.-B., Kunnavakkam, M.V., Houlihan, F.M., Schlax, M., Liddle, J.A., Kolodner, P., Nalamasu, O., Rodgers, J.A., 2004. Shape-controlled, high fill-factor microlens arrays fabricated by a 3D diffuser lithography and plastic replication method. Optics Express 12 (25), 6366–6371. https://doi.org/10.1364/OPEX.12.006366.

Chen, C., Liu, X., Chai, C., Lei, Z., 2021. Deep learning based one-shot optically-sectioned structured illumination microscopy for surface measurement. Optics Express 29 (3), 4010–4021. https://doi.org/10.1364/OE.415210.

Choi, H., Wadduwage, D.N., Tu, T.Y., Matsudaira, P., So, P.T.C., 2015. Three-dimensional image cytometer based on widefield structured light microscopy and high-speed remote depth scanning. Cytometry A 87, 49–60. https://doi.org/10.1002/CYTO.A.22584.

Chu, K.K., Mertz, J., Lim, D., 2008. Wide-field fluorescence sectioning with hybrid speckle and uniform-illumination microscopy. Optics Letters 33 (16), 1819–1821. https://doi.org/10.1364/OL.33.001819.

FitzGerrell, A.R., Dowski, E.R., Cathey, W.T., 1997. Defocus transfer function for circularly symmetric pupils. Applied Optics 36 (23), 5796–5804. https://doi.org/10.1364/AO.36.005796.

Ford, T.N., Lim, D., Mertz, J., 2012. Fast optically sectioned fluorescence HiLo endomicroscopy 17. https://doi.org/10.1117/1.JBO.17.2.021105.

Goodman, J.W., 2005. Introduction to Fourier optics. Roberts and Company publishers.

Heintzmann, R., Mertz, J., Ventalon, C., 2007. Dynamic speckle illumination microscopy with wavelet prefiltering. Optics Letters 32 (11), 1417–1419. https://doi.org/10.1364/OL.32.001417.

Helmchen, F., Denk, W., 2005. Deep tissue two-photon microscopy. Nature Methods 2 (12), 932–940. https://doi.org/10.1038/nmeth818.

Hopkins, H.H., 1955. The frequency response of a defocused optical system. Proc R Soc Lond A Math Phys Sci 231, 91–103. https://doi.org/10.1098/RSPA.1955.0158.

Hsiao, H., Lin, C.Y., Vyas, S., Huang, K.Y., Yeh, J.A., Luo, Y., 2021. Telecentric design for digital-scanning-based HiLo optical sectioning endomicroscopy with an electrically tunable lens. J Biophotonics 14, e202000335. https://doi.org/10.1002/JBIO.202000335.

Hu, Y., Liang, D., Wang, J., Xuan, Y., Zhao, F., Liu, J., Li, R., 2022. Background-free wide-field fluorescence imaging using edge detection combined with HiLo. J Biophotonics 15, e202200031. https://doi.org/10.1002/JBIO.202200031.

Jonkman, J., Brown, C.M., Wright, G.D., Anderson, K.I., North, A.J., 2020. Tutorial: guidance for quantitative confocal microscopy. Nature Protocols 15 (5), 1585–1611. https://doi.org/10.1038/s41596-020-0313-9.

S. Kang, I. Ryu, D. Kim, Kauh SK, High-speed three-dimensional surface profile measurement with the HiLo optical imaging technique, 2018. https://opg.optica.org/abstract.cfm?uri=copp-2-6-568 (accessed November 9, 2022).

Kole, T.P., Tseng, Y., Jiang, I., Katz, J.L., Wirtz, D., 2012. Depth-resolved cellular microrheology using HiLo microscopy. Biomedical Optics Express 3 (6), 1241–1255. https://doi.org/10.1364/BOE.3.001241.

Kuo, W.K., Lin, S.Y., Hsu, S.W., Yu, H.H., 2017. Fabrication and investigation of the bionic curved visual microlens array films. Opt Mater (Amst) 66, 630–639. https://doi.org/10.1016/J.OPTMAT.2017.03.020.

Lauterbach, M.A., Ronzitti, E., Sternberg, J.R., Wyart, C., Emiliani, V., 2015. Fast Calcium Imaging with Optical Sectioning via HiLo Microscopy. PLoS One 10, e0143681. https://doi.org/10.1371/JOURNAL.PONE.0143681.

Lim, D., Ford, T.N., Chu, K.K., Metz, J., 2011. Optically sectioned in vivo imaging with speckle illumination. HiLo Microscopy 16. https://doi.org/10.1117/1.3528656.

Lim, C.S., Hong, M.H., Kumar, A.S., Rahman, M., Liu, X.D., 2006. Fabrication of concave micro lens array using laser patterning and isotropic etching. Int J Mach Tools Manuf 46, 552–558. https://doi.org/10.1016/J.IJMACHTOOLS.2005.06.004.

Mertz, J., 2011. Optical sectioning microscopy with planar or structured illumination. Nature Methods 8 (10), 811–819. https://doi.org/10.1038/nmeth.1709.

Mertz, J., Kim, J., 2010. Scanning light-sheet microscopy in the whole mouse brain with HiLo background rejection 15. https://doi.org/10.1117/1.3324890.

Mertz, J., Ventalon, C., 2006. Dynamic speckle illumination microscopy with translated versus randomized speckle patterns. Optics Express 14 (16), 7198–7209. https://doi.org/10.1364/OE.14.007198.

Sanchez-Ortiga, E., Doblas, A., Preza, C., Saavedra, G., Shabani, H., 2018. Improvement of two-dimensional structured illumination microscopy with an incoherent illumination pattern of tunable frequency. Applied Optics 57 (7), B92–B101. https://doi.org/10.1364/AO.57.000B92.

S. Santos, K.K. Chu, D. Lim, N. Bozinovic, T.N. Ford, C. Hourtoule, A.C. Bartoo, S.K. Singh, J. Mertz, Optically sectioned fluorescence endomicroscopy with hybrid-illumination imaging through a flexible fiber bundle, 10.1117/1.3130266 14 (2009) 030502. 10.1117/1.3130266.

Schniete, J., Franssen, A., Dempster, J., Bushell, T.J., Amos, W.B., McConnell, G., 2018. Fast optical sectioning for widefield fluorescence mesoscopy with the mesolens based on hilo microscopy. Scientific Reports 8 (1), 1–10. https://doi.org/10.1038/s41598-018-34516-2.

Shi, R., Kong, L., 2021. Evaluating structured-illumination patterns in optimizing optical-sectioning of HiLo microscopy. J Phys D Appl Phys 54, 414001. https://doi.org/10.1088/1361-6463/AC153B.

Shi, R., Jin, C., Xie, H., Zhang, Y., Li, X., Li, X., Dai, Q., Kong, L., Kong, L., 2019. Multi-plane, wide-field fluorescent microscopy for biodynamic imaging in vivo. Biomedical Optics Express 10 (12), 6625–6635. https://doi.org/10.1364/BOE.10.006625.

Sohn, I.B., Choi, H.K., Noh, Y.C., Kim, J., Ahsan, M.S., 2019. Laser assisted fabrication of micro-lens array and characterization of their beam shaping property. Appl Surf Sci 479, 375–385. https://doi.org/10.1016/J.APSUSC.2019.02.083.

Stokseth, P.A., 1969. Properties of a defocused optical system. JOSA 59 (10), 1314–1321. https://doi.org/10.1364/JOSA.59.001314.

Ventalon, C., Mertz, J., 2005. Quasi-confocal fluorescence sectioning with dynamic speckle illumination. Optics Letters 30 (24), 3350–3352. https://doi.org/10.1364/OL.30.003350.

Wang, Z., Bovik, A.C., Sheikh, H.R., Simoncelli, E.P., 2004. Image quality assessment: From error visibility to structural similarity. IEEE Trans. Image Process. 13, 600–612. https://doi.org/10.1109/TIP.2003.819861.

Wilson, T., Juškaitis, R., Neil, M.A.A., 1997. Method of obtaining optical sectioning by using structured light in a conventional microscope. Optics Letters 22 (24), 1905–1907. https://doi.org/10.1364/OL.22.001905.

Yuan, W., Li, L.H., Lee, W.B., Chan, C.Y., 2018. Fabrication of Microlens Array and Its Application: A Review. Chinese Journal of Mechanical Engineering (english Edition) 31, 1–9. https://doi.org/10.1186/S10033-018-0204-Y/FIGURES/12.

Zhou, X., Bedggood, P., Metha, A., 2014. Improving high resolution retinal image quality using speckle illumination HiLo imaging. Biomedical Optics Express 5 (8), 2563–2579. https://doi.org/10.1364/BOE.5.002563.